Battery internal temperature estimation via a semilinear thermal PDE model☆

Dong Zhang [a],*, Satadru Dey [b], Shu-Xia Tang [c], Ross Drummond [d], Scott J. Moura [e]

[a] *Department of Mechanical Engineering, Carnegie Mellon University, Pittsburgh, PA, USA*
[b] *Department of Mechanical Engineering, Pennsylvania State University, State College, PA, USA*
[c] *Department of Mechanical Engineering, Texas Tech University, Lubbock, TX, USA*
[d] *Department of Engineering Science, University of Oxford, Oxford, UK*
[e] *Department of Civil and Environmental Engineering, University of California, Berkeley, CA, USA*

ARTICLE INFO

ABSTRACT

Accurate Lithium-ion (Li-ion) battery internal temperature information enables high-fidelity monitoring and safe operation in battery management systems, thus prevents thermal faults that could cause catastrophic failures. This paper proposes an online temperature estimation scheme for cylindrical Li-ion batteries based on a one-dimensional semilinear parabolic partial differential equation (PDE) model subject to in-domain and output uncertainties, using temperature measurements at the battery surface only. The thermal state observer design exploits PDE backstepping method, with a mild assumption on the Lipschitz continuity of the nonlinear heat generation rate. A sufficient condition on the Lipschitz constant to achieve exponential convergence is derived. Furthermore, when the thermal system uncertainties are present, an analytic bound on the temperature estimation error is formulated in the sense of spatial $\mathcal{L}_2$ norm, in terms of Lipschitz constant, design parameters, and bounds on system uncertainties. Simulation studies on various practical current profiles are demonstrated to illustrate the effectiveness of the proposed thermal estimation framework on a commercial cylindrical Li-ion battery cell.

1. Introduction

Due to the penetration of the electric vehicles (EV) and consumer electronics, lithium-ion (Li-ion) batteries are ubiquitous. The reason for this widespread penetration is that Li-ion batteries possess one of the best energy-to-weight ratios, exhibit no memory effect, and have low self-discharge when not in operation (Chaturvedi, Klein, Christensen, Ahmed, & Kojic, 2010). However, as batteries insert themselves more and more into our society, their operation is becoming increasingly safety critical, meaning that any battery failure can have an increasingly important impact upon systems of increasing size (Kim & Shin, 2011). One of the existing challenges that substantially impacts the battery safety and performance is its thermal instability. In particular, many cases of thermal runaways leading to fire and explosion of Li-ion batteries have been previously reported in Wang, Ping, Zhao, Chu, Sun, and Chen (2012). As well as safety issues, thermal effects have also been shown to be key factors in the rate of battery degradation (Broussely, Biensan, Bonhomme, Blanchard, Herreyre, Nechev, & Staniewicz, 2005; Wang, Liu, Hicks-Garner, Sherman, Soukiazian, Verbrugge, Tataria, Musser, & Finamore, 2011). Hence, in order to improve battery safety and longevity, it is crucial to develop thermal management strategies to alleviate the effects of temperature and prevent the drastic failure of the battery from happening. Moreover, recent work in Yang, Liu, and Wang (2021) demonstrates improved battery power and fast charging ability for Lithium-Iron Phosphate (LFP) cells operated at 60°C ambient condition. This high temperature is closer to a thermal runaway regime and the hot spots need to be monitored carefully. In light of the above concerns and recent advancements, this work proposes an online model-based algorithm for battery internal temperature estimation based on a high-fidelity semilinear thermal partial differential equation (PDE) model, using battery surface temperature measurements only.

Modeling of battery thermal performance has been extensively studied in the literature (Doughty, Butler, Jungst, & Roth, 2002). Comprehensive high-dimensional thermal models, e.g., Chen, Wan, and Wang (2005), Kim, Pesaran, and Spotnitz (2007) and Song and Evans (2000), provide an accurate and thorough

---

understanding of the cell temperature behavior from an electro-chemical point of view. Nevertheless, since these high-dimensional models are too complicated and demand a great amount of computational power, their application to real-time estimation and control in a battery management system (BMS) will not be feasible for applications outside of industrial/stationary storage (Dey, Biron, Tatipamula, Das, Mohon, Ayalew, & Pisu, 2016). To balance physical relevance and model structural simplicity, reduced-order PDE thermal models have been proposed (Al Hallaj, Maleki, Hong, & Selman, 1999; Gu & Wang, 2000; Muratori, Canova, & Guezennec, 2012). A few other finite-dimensional approaches for battery thermal modeling stand out, and one such model is a two-state thermal model that predicts the surface and core temperature of a cylindrical battery cell (Park & Jaura, 2003; Zhang, Couto, Park, Gill, & Moura, 2020b). A lumped thermal model has also been proposed by Smith et al. in Smith and Wang (2006). Note that battery thermal behavior exhibits certain nonlinearity that are originated from resistive heat generation rate, reversible entropic heat, and enthalpy of reactions, etc.

Catastrophic thermal failures stimulate numerous works on the development of thermal management strategies. Previous studies on battery state estimation can be categorized into two main groups, i.e., the equivalent circuit model-based estimation (Hu & Yurkovich, 2012; Plett, 2004; Zhang, Dey, Perez, & Moura, 2017, 2019b) and the electrochemical model-based estimation (Dey, Ayalew, & Pisu, 2015; Klein, Chaturvedi, Christensen, Ahmed, Findeisen, & Kojic, 2013; Moura, Argomedo, Klein, Mirtabatabaei, & Krstic, 2017; Tang, Camacho-Solorio, Wang, & Krstic, 2017; Zhang, Dey, Couto, & Moura, 2019a). The existing BMS generally uses a thermal sensor attached to the surface of the cell to measure surface temperature. As such, in Lin, Perez, Siegel, Stefanopoulou, Li, Anderson, Ding, and Castanier (2013), an adaptive observer for battery core temperature estimation was designed for a two-state thermal model using surface measurements. As well as estimation, studies on thermal fault diagnosis, e.g., the detection and isolation of the faults that influence the surface and core temperature in the two-state thermal model (Dey et al., 2016) and a PDE observer based fault detection (Dey, Perez, & Moura, 2019), have also demonstrated benefits. A dual Kalman filter based temperature distribution estimation for cylindrical batteries under unknown cooling, based on a reduced radially distributed one-dimensional thermal modeling, was proposed in Kim, Mohan, Siegel, Stefanopoulou, and Ding (2014). More work on cylindrical cell internal temperature distribution estimation by combining measured electrochemical impedance and surface temperature, relying on a combined thermal-impedance model is introduced in Richardson, Ireland, and Howey (2014). However, these methodologies suffer from one or more of the following drawbacks: (i) Early lumping approaches, where the thermal PDE models are discretized and approximated by systems of ordinary differential equations (ODE) a priori, are used to design the observers. This leads to the loss of the physical significance of the PDE models and of the phenomena that they represent, and the state estimates from the discretized systems may not always converge to the true states; (ii) Only a small portion of these works provide theoretically certified convergence properties for the proposed estimation scheme; (iii) Last but not the least, most of these works do not consider the inherent nonlinearity of battery thermal model. Hence, this paper attempts to collectively address these challenges and research gaps by proposing a provably convergent observer directly on the high-fidelity nonlinear thermal PDE model.

Methods for control/estimation of linear parabolic PDEs with late lumping have been well studied. The stabilization of unstable heat equations using boundary observation was addressed

in Nambu (1984) by means of an auxiliary functional observer. Smyshlyaev et al. apply the backstepping method to controller design for a model with space-dependent diffusivity or time-dependent reactivity (Smyshlyaev & Krstic, 2005). The techniques introduced in Smyshlyaev and Krstic (2010) provide a thorough analysis of the stability of adaptive control for linear parabolic PDEs with spatially varying coefficients. However, extending these results from linear to nonlinear PDEs require a more intricate analysis, with only few attempts so far. For instance, an extended Luenberger observer is developed for a class of semilinear parabolic PDEs in Meurer (2013). It verifies the exponential stability of the linearized observer error dynamics, in which the design extends the well-known backstepping method (Krstic & Smyshlyaev, 2008) to include the Volterra transformation with a time-dependent kernel function. A series of studies by Vazquez et al. discuss the control design for a 1-D parabolic PDE with Volterra nonlinearities (Vazquez & Krstic, 2008a, 2008b). Boundary controller have also been designed towards Burgers' equation (Krstic, 1999). Additionally, designs based upon the plant models with modeling and parametric uncertainties, have also been explored. Cheng considers the stabilization of the heat equation with parameter variation and boundary uncertainties by designing a sliding mode controller (Cheng, Radisavljevic, & Su, 2011). Parabolic PDEs that are subject to in-domain and boundary parameter uncertainties are examined in Ahmed-Ali, Giri, Krstic, Burlion, and Lamnabhi-Lagarrigue (2016), Zhang, Tang, and Moura (2019c). However, none of the aforementioned works discuss observer design for semilinear parabolic PDE systems simultaneously subjected to Lipschitz nonlinearity and model uncertainties.

In this context, we advance the aforementioned works by developing a provably convergent PDE observer for Li-ion battery thermal estimation, with the only measurement from the battery cell surface. The thermal dynamics for a cylindrical battery in the radial direction can be described by a one-dimensional semilinear parabolic PDE with a mixture of Neumann and Robin boundary conditions. Provided that the nonlinear in-domain heat generation rate is Lipschitz continuous, this work marks one of the first to simultaneously consider PDE model nonlinearity, in-domain modeling uncertainty, and boundary measurement uncertainty within a single observer design framework, which addresses several key practical challenges often faced within EV applications (i.e., in-situ modeling and measurement uncertainties). This problem is challenging because the conventional PDE backstepping control and estimation techniques (Krstic & Smyshlyaev, 2008) are well suited for linear PDEs without modeling uncertainties. This paper meets these challenges by deriving an analytical expression for the nonlinear estimation error in the sense of $\mathcal{L}_2$ norm in terms of observer gains, Lipschitz constant, and bounds on the uncertainties, and further proposing an optimization problem to achieve robust estimation by minimizing the size of the derived bound. In this paper, we choose to adopt the PDE backstepping method due to its unique feature to eliminate in-domain destabilizing terms using control and observations only on the boundary. This makes it a suitable method for battery internal temperature distribution estimation from surface temperature measurements only. It is further noted that although the observer design for a general nonlinear PDE remains an unsolved problem, this paper offers a new and different perspective on state observer for a class of semilinear PDE subject to Lipschitz continuous nonlinearity with respect to Meurer (2013). The proposed state estimation approach does not require an extended linearization with respect to the estimated state during observer design and convergence analysis. The design is unique, since it exploits fundamental thermal dynamic properties and adopts a

high-fidelity thermal model for the purpose of battery temperature monitoring, which ultimately enhances battery safety and longevity in EV applications.

The remainder of the paper is organized as follows. Section 2 formulates the one-dimensional semilinear thermal PDE model with nonlinear Lipschitz continuous heat generation rate. Section 3 presents the state estimation scheme based on the preceding model without the in-domain and output uncertainties, and the corresponding stability analysis of the estimation error dynamics. Section 4 proposes the strategies for observer gain selection. Section 5 develops a robust state estimation for the plant model with in-domain and output uncertainties. The performance of the observers is demonstrated via simulations in Section 6. The conclusions and future works are discussed in Section 7.

Notation. Throughout the manuscript, $T(x, t)$ denotes the plant's state variable, which depends on nondimensionalized space x and time t. The x and t subscripts represent partial derivatives with respect to the notated variable: $u_t = \partial u/\partial t$, $u_x = \partial u/\partial x$, and $u_{xx} = \partial^2 u/\partial x^2$. The dot symbol denotes derivative with respect to time t, e.g., $\dot{u} = \mathrm{d}u/\mathrm{d}t$. The spatial $\mathcal{L}_2$ norm is defined as

$$\|T(\cdot, t)\| = \sqrt{\int_0^1 T^2(x, t)\mathrm{d}x}.$$

2. Distributed parameter thermal model

This section presents the development of a one-dimensional nonlinear PDE thermal model for batteries, oriented towards state estimation design.

2.1. One-dimensional thermal model

For a sufficiently long cylindrical battery cell, the heat transfer resistance of spirally wound in the axial direction is significantly smaller than that in the radial direction, which allows to model the thermal dynamics using radial heat transfer only (Al Hallaj et al., 1999; Evans & White, 1989). Furthermore, the Biot number in the radial direction is sufficiently large such that the temperature gradients are not negligible. As such, the following one-dimensional thermal model for the radially distributed temperature profile of a cylindrical battery cell is adopted from Al Hallaj et al. (1999). By assuming that heat is generated uniformly throughout the cell, the cell can be treated as a thermally homogeneous body:

$$\frac{1}{\alpha}\frac{\partial \overline{T}}{\partial \overline{t}}(r, \overline{t}) = \frac{\partial^2 \overline{T}}{\partial r^2}(r, \overline{t}) + \frac{1}{r}\frac{\partial \overline{T}}{\partial r}(r, \overline{t}) + \frac{\dot{Q}(r, \overline{t})}{\overline{k}}, \tag{1}$$

$$\frac{\partial \overline{T}}{\partial r}(0, \overline{t}) = 0, \tag{2}$$

$$\frac{\partial \overline{T}}{\partial r}(R_c, \overline{t}) = \frac{\overline{h}}{\overline{k}}(T_\infty - \overline{T}(R_c, \overline{t})), \tag{3}$$

$$y_m(t) = \overline{T}(R_c, \overline{t}), \tag{4}$$

where $\overline{T}(r, \overline{t})$ is the battery temperature distribution with respect to radial position and time. $r \in [0, R_c]$ represents the radial coordinate, R_c is the battery radius, and $\overline{t} \in \mathbb{R}^+$ is time. T_∞ is ambient temperature, and $\dot{Q}$ denotes the volumetric heat generation rate. Moreover, parameters $\overline{k}$ and $\overline{h}$ are the thermal conductivity and effective surface heat transfer coefficient of the battery cell, respectively. Convective cooling through the battery surface is modeled by a Robin boundary condition in (3). In addition, $\alpha = \overline{k}/(DC_p)$ is the thermal diffusivity, where D is the mass density and C_p denotes the specific heat capacity. Furthermore, in (4), it is assumed that the only temperature measurements are from the

battery surface (system boundary). This is a standard practice as the cell internal temperature measurement is intractable and may lead to danger.

A coordinate transformation and normalization is now performed to simplify the structure of the model and translate it into a form for which an observer can be derived. First, we transform the system (1)–(4) from the cylindrical to Cartesian coordinates with spatial variable $\overline{x}$. The coordinates and parameters are then normalized by defining $x = \overline{x}/R_c$, $t = \alpha\overline{t}/R_c^2$, $k = \overline{k}/R_c^2$, $h = \overline{h}/R_c$, $T(x, t) = \overline{T}(r, \overline{t})$ to give the following PDE system:

$$\frac{\partial T}{\partial t}(x, t) = \frac{\partial^2 T}{\partial x^2}(x, t) + \frac{\dot{Q}(x, t)}{k}, \tag{5}$$

with boundary conditions

$$\frac{\partial T}{\partial x}(0, t) = 0, \tag{6}$$

$$\frac{\partial T}{\partial x}(1, t) = \delta(T_\infty - T(1, t)), \tag{7}$$

where $x \in [0, 1]$ and $\delta = h/k$. The surface temperature measurement signal in the transformed coordinate becomes

$$y_m(t) = T(1, t). \tag{8}$$

The formula for computing heat generation rate proposed by Bernardi, Pawlikowski, and Newman (1985) is employed frequently in its simplified form (Dey et al., 2019; Forgez, Do, Friedrich, Morcrette, & Delacourt, 2010):

$$\dot{Q}(x, t) = I^2(t)R_s(T(x, t), z(t)) - I(t)T(x, t)\frac{\partial V_{oc}}{\partial T}, \tag{9}$$

where $I(t)$ is the applied current, $z(t)$ represents battery state of charge (SOC), and V_{oc} denotes open circuit voltage. Symbol R_s stands for volumetric battery internal resistance and is generally dependent on battery temperature and SOC (Lin et al., 2013; Samad, Siegel, & Stefanopoulou, 2014). The term $R_s(T(x, t), z(t))$ can be characterized experimentally, e.g., see Fig. 6 in Samad et al. (2014) for an illustrative example. For the heat generation rate expression in (9), the first term is the heat generated from resistive dissipation, which is always positive. The second term is the reversible entropic heat Keyser, Pesaran, Li, Santhanagopalan, Smith, Wood, Ahmed, Bloom, Dufek, Shirk, et al. (2017), Thomas and Newman (2003). The entropic coefficient $(\partial V_{oc}/\partial T)$ varies with SOC and can be determined by offline experimental studies, e.g., see Forgez et al. (2010).

Remark 1. It is worth noting that tabs in cylindrical cells could lead to heterogeneity in current distribution and hence temperature under high current density. The thermal model (1)–(9) does not specifically consider this effect, because the unsteady-state one-dimensional (radial direction) thermal model with lumped properties are sufficient for modeling purposes under normal conditions of battery use (Al Hallaj et al., 1999). Besides, the choice of the one-dimensional thermal model intelligently strikes a balance between modeling accuracy and tractability towards state observer design. Furthermore, exemplified by the development of Tesla's forthcoming tabless 4860 cells, it is expected that the thermal gradient will be less severe than current cell designs. As such, the restrictiveness of the assumption to neglect the heat generation around the tabs may be less severe in future battery packs (Tranter, Timms, Shearing, & Brett, 2020).

2.2. Model reduction and analysis

In this work, the heat generation rate formulation (9) is simplified by neglecting the entropic heat generation in the subsequent discussions as the entropic coefficient $(\partial V_{oc}/\partial T)$ is significantly

small for certain types of cell chemistry, e.g., LFP cell (Forgez et al., 2010). The simplified heat generation rate is adopted, which is used to strike a balance between the need for a model of sufficient accuracy yet is simple enough to enable observer design with convergence guarantees. Furthermore, the simplified heat generation rate is considered to be sufficient for electric vehicle and portable electronics applications (Du, Hu, Xie, Hu, Zhang, & Lin, 2020), and its dependence on temperature and SOC further enhances the prediction accuracy for cells over a wide range of operational conditions (for instance, various current rates and different temperatures).

Remark 2. As noted in Käbitz, Gerschler, Ecker, Yurdagel, Emmermacher, André, Mitsch, and Sauer (2013), Liaw, Roth, Jungst, Nagasubramanian, Case, and Doughty (2003) and Lin et al. (2013) the behavior of R_s due to the variation in temperature should nearly follow an Arrhenius type relationship:

$$R_s(T, z) = M(z) \cdot R_{s,\text{ref}} \exp\left[\frac{E_a}{R}\left(\frac{1}{T} - \frac{1}{T_{\text{ref}}}\right)\right], \tag{10}$$

where T_{ref} is a given reference temperature, E_a is activation energy, R denotes universal gas constant, and $R_{s,\text{ref}} = R_s(T_{\text{ref}})$. $M(z) > 0$ is usually a nonlinear function. Such a monotonically decreasing Arrhenius expression is retrieved from Lin et al. (2013). Function $M(z)$ characterizes the nonlinear dependence on SOC (Lin, Perez, Mohan, Siegel, Stefanopoulou, Ding, & Castanier, 2014). Observe that the gradient of R_s with respect to T is

$$\frac{dR_s}{dT} = -M(z) \cdot R_{s,\text{ref}}\frac{E_a}{RT^2} \exp\left[\frac{E_a}{R}\left(\frac{1}{T} - \frac{1}{T_{\text{ref}}}\right)\right] < 0. \tag{11}$$

Li-ion battery manufacturers specify safety restrictions on allowable operation temperature range, which is generally between $-30\,°C$ (243.15 K) and 60 °C (333.15 K) for typical Li-ion battery operation (Koniak & Czerepicki, 2017). Within this temperature range, the function dR_s/dT in (11) is monotonically increasing with respect to T. Hence, suppose the maximum and minimum temperature regulated by an application are T_{max} and T_{min}, we have

$$\frac{dR_s}{dT}(T_{\text{min}}, z) \leq \frac{dR_s}{dT}(T, z) \leq \frac{dR_s}{dT}(T_{\text{max}}, z) < 0, \tag{12}$$

for all $z \in [0, 1]$.

Consequently, the modeling error from the aforementioned reductions on heat generation is compensated by an in-domain uncertainty $v(x, t)$, i.e.,

$$\dot{Q}(x, t) = I^2 R_s(T(x, t), z(t)) + v(x, t), \tag{13}$$

where $v(x, t)$ is upper and lower bounded, and these bounds can be numerically retrieved by experiments. Hence, substituting the reduced-order heat generation rate (13) into the dynamics (5) yields the plant model under consideration in the subsequent studies:

$$\frac{\partial T}{\partial t}(x, t) = \frac{\partial^2 T}{\partial x^2}(x, t) + f(T(x, t), z(t)) + \varepsilon(x, t), \tag{14}$$

where $\varepsilon(x, t) = v(x, t)/k$ and

$$f(T(x, t), z(t)) = \frac{1}{k}I^2 R_s(T(x, t), z(t)), \tag{15}$$

with R_s given by (10). The boundary conditions are

$$\frac{\partial T}{\partial x}(0, t) = 0, \tag{16}$$

$$\frac{\partial T}{\partial x}(1, t) = \delta(T_\infty - T(1, t)). \tag{17}$$

The initial condition of the plant model is $T(x, 0) = T_0(x)$. For the design of the state observer, the temperature at the surface of the battery is measured:

$$y(t) = T(1, t) + \mu(t), \tag{18}$$

where we impose output uncertainty $\mu(t)$ to account for disturbances from ambient environment and thermal sensor inaccuracies. Let $\mathcal{U} = \mathcal{L}_2(T_{\text{min}}, T_{\text{max}})$ denote the state space of $T(x, t)$. According to (10), $R_s(T, z)$ is C^1 in T, for all $z \in [0, 1]$ and $T \in \mathcal{U}$. Furthermore, since function $f(T, z)$ satisfies (15), $f(T, z)$ is also C^1 in T. The next theorem establishes Lipschitz continuity of function $f(T, z)$.

Theorem 1 (*Lipschitz Continuity*). *The nonlinear function $f : \mathcal{U} \times [0, 1] \to \mathcal{U}$ is Lipschitz continuous with respect to T in the range $T \in [T_{\text{min}}, T_{\text{max}}]$. That is, for all $T_1, T_2 \in \mathcal{U}$, there exists a positive constant $\Gamma = \Gamma(z)$ such that*

$$\|f(T_1, z) - f(T_2, z)\| \leq \Gamma(z) \cdot \|T_1 - T_2\| \tag{19}$$

holds for all $z \in [0, 1]$ and $t \in [0, \infty)$. Moreover, let $\gamma = \max_z(\Gamma(z)) > 0$ which is independent of z, then γ can be regarded as the Lipschitz constant for function $f(T, z)$.

Practically, a candidate for the Lipschitz constant may be obtained by computing the infinity norm of (df/dT). According to (15) and Remark 2,

$$\gamma = \left\|\frac{df}{dT}\right\|_\infty = \frac{1}{k}|I|_{\text{max}}^2\left|\frac{dR_s}{dT}(T, z)\right|_{\text{max}}$$

$$= \sigma \cdot \exp\left[\frac{E_a}{R}\left(\frac{1}{T_{\text{min}}} - \frac{1}{T_{\text{ref}}}\right)\right], \tag{20}$$

where $\sigma = |M(z)|_{\text{max}}|I|_{\text{max}}^2 R_{s,\text{ref}}E_a/(kRT_{\text{min}}^2)$. Herein, $|\cdot|_{\text{max}}$ denotes the absolute maximum value.

Theorem 2. *Theorem 1 guarantees the existence and uniqueness of a classical solution to the PDE system (14)–(17).*

Proof. It is observed from (9) and (13) that v (or equivalently ε) is globally Lipschitz continuous with respect to T in the range $T \in [T_{\text{min}}, T_{\text{max}}]$. Hence, the function $F := f + \varepsilon$ is also globally Lipschitz continuous with respect to T in the range $T \in [T_{\text{min}}, T_{\text{max}}]$. According to Meurer (2013, Assumption 1) and Pazy (2012, Theorem 6.1.5), the existence and uniqueness of a classical solution can be ensured.

Assumption 1. The in-domain uncertainty $\varepsilon(x, t)$ is finite and bounded by $\varepsilon(x, t) \leq \bar{\varepsilon}, \forall(x, t) \in [0, 1] \times [0, \infty)$, where $\bar{\varepsilon} \geq 0$. The disturbance $\mu(t)$ in the output equation is finite and bounded by $\mu(t) \leq \bar{\mu}, \forall t \in [0, \infty)$, where $\bar{\mu} \geq 0$. We further assume that $\mu(t)$ is continuously differentiable with respect to time t.

Our objective is to design a provably convergent observer to estimate battery radially distributed temperature profile $T(x, t)$ by utilizing only cell's surface temperature measurements $y(t) = T(1, t)$. As such, in Section 3, we first present an observer design and the corresponding observer convergence analysis based on the uncertainty-free plant model, i.e., $\varepsilon(x, t) = 0$ and $\mu(t) = 0$, $\forall x \in [0, 1]$ and $t \in [0, \infty)$. Furthermore, in Section 5, we develop a robust state estimation scheme based on the plant model with uncertainties, i.e., $\varepsilon(x, t) \neq 0$ and $\mu(t) \neq 0$, in the sense of minimizing the estimation error via optimal observer gain scheduling.

3. State estimation for uncertainty-free plant model

In this section, the following uncertainty-free thermal plant model, namely $\varepsilon(x, t) = 0$ and $\mu(t) = 0$, for all $x \in [0, 1]$ and $t \in [0, \infty)$, is considered:

$$T_t(x, t) = T_{xx}(x, t) + f(T(x, t), z(t)), \tag{21}$$

$$T_x(0, t) = 0, \tag{22}$$

$$T_x(1, t) = \delta(T_\infty - T(1, t)), \tag{23}$$

$$T(x, 0) = T_0(x), \tag{24}$$

$$y(t) = T(1, t). \tag{25}$$

An observer for reconstructing the spatial and temporal evolution of cell temperature is proposed in the subsequent sections.

3.1. State observer structure

A distributed parameter state observer system is designed by using a copy of the plant model with output error injection,

$$\widehat{T}_t(x, t) = \widehat{T}_{xx}(x, t) + f(\widehat{T}(x, t), z(t))$$
$$+ p_1(x)\big[y(t) - \widehat{T}(1, t)\big], \tag{26}$$

$$\widehat{T}_x(0, t) = 0, \tag{27}$$

$$\widehat{T}_x(1, t) = \delta(T_\infty - \widehat{T}(1, t)) + p_{10}\big[y(t) - \widehat{T}(1, t)\big], \tag{28}$$

$$\widehat{T}(x, 0) = \widehat{T}_0(x) \neq T_0(x), \tag{29}$$

where $\widehat{T}(x, t)$ denotes the estimation of $T(x, t)$, and $\widehat{T}(1, t)$ is the boundary state estimate. Symbols $p_1(x)$ and p_{10} are spatially varying and constant observer gains to be designed to guarantee the stability of the estimation error $\widetilde{T}(x, t) := T(x, t) - \widehat{T}(x, t)$.

Remark 3. In this paper, we assume that the SOC of the battery is either known or can be reliably estimated in real time by algorithms developed in, e.g., Dey et al. (2015), Hu and Yurkovich (2012), Klein et al. (2013), Moura et al. (2017), Plett (2004), Tang et al. (2017) and Zhang et al. (2019a, 2017, 2019b). The estimated SOC is then used to evaluate function f in the observer dynamics (26).

Subtracting (26)–(29) from (21)–(24) yields the estimation error dynamics:

$$\widetilde{T}_t(x, t) = \widetilde{T}_{xx}(x, t) + \phi(x, t) - p_1(x)\widetilde{T}(1, t), \tag{30}$$

$$\widetilde{T}_x(0, t) = 0, \tag{31}$$

$$\widetilde{T}_x(1, t) = -(\delta + p_{10})\widetilde{T}(1, t), \tag{32}$$

$$\widetilde{T}(x, 0) = T(x, 0) - \widehat{T}(x, 0), \tag{33}$$

where

$$\phi(x, t) := f(T(x, t), z(t)) - f(\widehat{T}(x, t), z(t)). \tag{34}$$

Although the explicit dependence of $\phi(x, t)$ on $T(x, t)$ and $\widehat{T}(x, t)$ is suppressed in the notation above, this explicit dependence remains, and is crucial, in the subsequent error system stability analysis.

3.2. Backstepping transformation

To determine the appropriate observer gains, we adopt the backstepping approach (Krstic & Smyshlyaev, 2008). We seek a linear backstepping transformation, i.e., a Volterra integral transformation, that transforms the state of the error system $\widetilde{T}(x, t)$ to a target state $\omega(x, t)$, by making use of the following expression with kernel function $K(x, y)$:

$$\widetilde{T}(x, t) = \omega(x, t) - \int_x^1 K(x, y)\omega(y, t)\mathrm{d}y, \tag{35}$$

which maps the error system (30)–(32) to the target system

$$\omega_t(x, t) = \omega_{xx}(x, t) + \psi(x, t) - c\omega(x, t), \tag{36}$$

$$\omega_x(0, t) = 0, \tag{37}$$

$$\omega_x(1, t) = -(c_1 + \delta)\omega(1, t), \tag{38}$$

where constants c and c_1 are parameters to be designed. Moreover, $\psi(x, t)$ is the transformed function from $\phi(x, t)$ by the same backstepping transformation structure in (35) Cheng et al. (2011), as follows,

$$\phi(x, t) = \psi(x, t) - \int_x^1 K(x, y)\psi(y, t)\mathrm{d}y. \tag{39}$$

To explicitly determine the kernel function $K(x, y)$ we differentiate both sides of the transformation in (35) with respect to x and t and take the target system dynamics (36)–(38) into account. An example of a similar procedure can be retrieved in Krstic and Smyshlyaev (2008, Chapter 4). The computation reveals that the kernel function $K(x, y)$ must satisfy the following Klein–Gordon PDE,

$$K_{xx}(x, y) - K_{yy}(x, y) = -cK(x, y), \tag{40}$$

$$K_x(0, y) = 0, \tag{41}$$

$$K(x, x) = -\frac{c}{2}x, \tag{42}$$

in which the boundary condition (41) emerges from evaluating (35) together with the boundary conditions (31)–(32). A unique and closed-form analytic solution exists for the PDE (40)–(42):

$$K(x, y) = -cy\frac{I_1\big(\sqrt{c(y^2 - x^2)}\big)}{\sqrt{c(y^2 - x^2)}}, \tag{43}$$

where $I_1(\cdot)$ is the modified Bessel function of the first kind. Solution (43) is derived by converting the PDE (40)–(42) into an integral equation and applying the method of successive approximations. Moreover, the observer gains are computed as

$$p_1(x) = -K_y(x, 1) - (c_1 + \delta)K(x, 1), \tag{44}$$

$$p_{10} = c_1 - K(1, 1) = c_1 + \frac{c}{2}. \tag{45}$$

Therefore, the observer gains (44)–(45) can be determined offline utilizing the kernel PDE solution (43).

Remark 4. The fact that $\psi(x, t)$ is the transformed version of $\phi(x, t)$ under the same backstepping transformation used for estimation error state transformation makes the kernel PDE (40)–(42) to exhibit the same structure as that of the linear case, e.g., Krstic and Smyshlyaev (2008, Chapter 4). The challenge hereafter lies in the stability verification of the target system (36)–(38).

Additionally, it is necessary to verify the existence and uniqueness of the inverse backstepping transformation, so that the stability of the target system implies the stability of the original error system. Consider the inverse backstepping transformation (Krstic & Smyshlyaev, 2008),

$$\omega(x, t) = \widetilde{T}(x, t) + \int_x^1 \ell(x, y)\widetilde{T}(y, t)\mathrm{d}y, \tag{46}$$

with the kernel function $\ell(x, y)$. Similarly, differentiating both sides of the inverse backstepping transformation with respect to x and t yields the kernel PDE for $\ell(x, t)$:

$$\ell_{xx}(x, y) - \ell_{yy}(x, y) = c\ell(x, y), \tag{47}$$

$$\ell_x(0, y) = 0, \tag{48}$$

$$\ell(x, x) = -\frac{c}{2}x, \tag{49}$$

which has an analytic solution of the form

$$\ell(x, y) = -cy \frac{J_1\left(\sqrt{c(y^2 - x^2)}\right)}{\sqrt{c(y^2 - x^2)}}, \tag{50}$$

where $J_1(\cdot)$ is the Bessel function of the first kind.

3.3. Stability of the target system

Based on the analysis in Section 3.2, the analytic solutions for the backstepping and inverse backstepping kernel functions $K(x, y)$ and $\ell(x, y)$ exist and are unique. Therefore, the stability properties of the target system (36)–(37) imply the stability of the original error system (30)–(32). In this section, we perform Lyapunov analysis to establish the stability of the target system in the sense of spatial $\mathcal{L}_2$ norm. Prior to that, we first present and prove the following lemma.

Lemma 1. *The nonlinear function $\psi(x, t)$ in the target system (36) verifies the following inequality for all $t \in [0, \infty)$,*

$$\|\psi(\cdot, t)\| \leq \kappa(c; \gamma) \|\omega(\cdot, t)\|, \tag{51}$$

with $\kappa(c; \gamma) := \gamma[1 + \rho(c)][1 + \eta(c)]$, where

$$\rho(c) := \sqrt{\int_0^1 \int_x^1 \ell^2(x, y; c) \mathrm{d}y \mathrm{d}x}, \tag{52}$$

$$\eta(c) := \sqrt{\int_0^1 \int_x^1 K^2(x, y; c) \mathrm{d}y \mathrm{d}x}, \tag{53}$$

and c is the design variable of the target system in (36).

Proof. The inverse backstepping transformation from $\psi(x, t)$ to $\phi(x, t)$ specified by the kernel function $\ell(x, y)$ in (50) is written as

$$\psi(x, t) = \phi(x, t) + \int_x^1 \ell(x, y)\phi(y, t)\mathrm{d}y. \tag{54}$$

Applying the triangle inequality produces

$$\|\psi(x, t)\| \leq \|\phi(x, t)\| + \left\| \int_x^1 \ell(x, y)\phi(y, t)\mathrm{d}y \right\|$$

$$= \|\phi(x, t)\| + \sqrt{\int_0^1 \left(\int_x^1 \ell(x, y)\phi(y, t)\mathrm{d}y \right)^2 \mathrm{d}x}$$

$$\leq \|\phi(x, t)\| + \sqrt{\int_0^1 \left(\int_x^1 \ell^2(x, y)\mathrm{d}y \int_x^1 \phi^2(y, t)\mathrm{d}y \right) \mathrm{d}x}$$

$$\leq \|\phi(x, t)\| + \sqrt{\int_0^1 \left(\int_x^1 \ell^2(x, y)\mathrm{d}y \right) \|\phi(x, t)\|^2 \mathrm{d}x}$$

$$= \left(1 + \sqrt{\int_0^1 \int_x^1 \ell^2(x, y)\mathrm{d}y\mathrm{d}x} \right) \|\phi(x, t)\|$$

$$\leq \gamma \left(1 + \sqrt{\int_0^1 \int_x^1 \ell^2(x, y)\mathrm{d}y\mathrm{d}x} \right) \|\widetilde{T}(x, t)\|, \tag{55}$$

where the second inequality originates from the Cauchy–Schwarz inequality, and the last inequality stems from the Lipschitz continuity of function f in Theorem 1. A similar computation can be performed based on the forward backstepping transformation (35) to conclude

$$\|\widetilde{T}(x, t)\| \leq \left(1 + \sqrt{\int_0^1 \int_x^1 K^2(y, t)\mathrm{d}y\mathrm{d}x} \right) \|\omega(x, t)\|. \tag{56}$$

Therefore, in view of (55) and (56), function $\psi(x, t)$ verifies the inequality $\|\psi(\cdot, t)\| \leq \kappa(c; \gamma)\|\omega(\cdot, t)\|$.

Through Lemma 1, the stability of the error system (30)–(34) in terms of the $\mathcal{L}_2$ norm can then be established via the stability of the target system.

Theorem 3 (*Convergence of State Observer*). *Consider the observer error dynamics (30)–(34), and let the observer gains $p_1(x)$ and p_{10} be as in (44) and (45). Given Lipschitz constant γ, if the design parameters c and c_1 are chosen such that*

$$c > \kappa(c; \gamma) - \frac{1}{4}, \qquad c_1 \geq \frac{1}{2} - \delta, \tag{57}$$

then the origin of the error dynamics $\widetilde{T}(x, t) = 0$ is exponentially stable in the sense of $\mathcal{L}_2$ norm, without the presence of the in-domain uncertainty and the output uncertainty, i.e., $\varepsilon(x, t) = 0$ and $\mu(t) = 0$ for all $x \in [0, 1]$ and $t \in [0, \infty)$.

Proof. Consider the Lyapunov functional candidate for system (36)–(39):

$$W_1(t) = \frac{1}{2} \int_0^1 \omega^2(x, t)\mathrm{d}x = \frac{1}{2} \|\omega(x, t)\|^2. \tag{58}$$

The time derivative of the Lyapunov function $W_1(t)$ along the state trajectory can be computed as

$$\dot{W}_1 = \int_0^1 \omega(x, t)\omega_t(x, t)\mathrm{d}x$$

$$= \int_0^1 \omega\omega_{xx}\mathrm{d}x + \int_0^1 \omega\psi\,\mathrm{d}x - c\int_0^1 \omega^2\mathrm{d}x. \tag{59}$$

Applying the integration by parts to the first term, and Cauchy–Schwarz inequality to the second term at the right-hand side of (59) result in

$$\dot{W}_1 \leq -(c_1 + \delta)\omega^2(1, t) - \|\omega_x\|^2 + \|\psi\|\|\omega\| - c\|\omega\|^2. \tag{60}$$

Applying Poincaré inequality, $-\|\omega_x\|^2 \leq \frac{1}{2}\omega^2(1) - \frac{1}{4}\|\omega\|^2$, to the second term at the right-hand side of (60), and substituting the third term with (51), yields

$$\dot{W}_1 \leq -\left(c_1 + \delta - \frac{1}{2} \right)\omega^2(1) - \left[c + \frac{1}{4} - \kappa(c; \gamma) \right]\|\omega\|^2. \tag{61}$$

If the design parameters are chosen such that $c_1 \geq \frac{1}{2} - \delta$ and $c > \kappa(c; \gamma) - \frac{1}{4}$, (61) is simplified to

$$\frac{\mathrm{d}}{\mathrm{d}t}\|\omega\| \leq -\left[c + \frac{1}{4} - \kappa(c; \gamma) \right]\|\omega\|, \tag{62}$$

which confirms the exponential stability of $\omega(x, t)$, as well as $\widetilde{T}(x, t)$, in the sense of $\mathcal{L}_2$ norm.

Remark 5. The state observer design imposes a simple linear output error injection for a nonlinear plant model, without having to perform linearization and compute time-varying kernel functions as in Meurer (2013). However, its limitation is analogous to that of observer design for Lipschitz nonlinear ODE system (Rajamani, 1998), which will be discussed in the next section.

4. Numerical selection of design parameters

The design criteria (57) for the stability of the origin of the error system enforces c_1 to be greater than a fixed constant $(1/2 - \delta)$, and an affine function of c to be greater than a nonlinear function $\kappa(c; \gamma)$. It should be highlighted that for a Lipschitz constant γ, $\kappa(c; \gamma)$ increases near exponentially with respect to c since the backstepping kernel function $K(x, y)$ is dependent

on the modified Bessel function $I_1(\cdot)$. The conditions in (57) essentially require a linear function to dominate an exponential function, no matter that the argument of function $I_1(\cdot)$ in (43) is a square root of c. Satisfaction of the condition in (57) is then entirely dependent upon the Lipschitz bound of the nonlinearity γ. A numerical study is now presented to explore the space of γ for which a feasible solution to the inequality of (57) exists.

Fig. 1 provides the visualization for the affine function $(c + 1/4)$ and the nonlinear function $\kappa(c; \gamma)$ with respect to c. As an illustrative example, when $\gamma < \gamma^*$, $\kappa(c; \gamma)$ (the black solid line) intersects with $(c + 1/4)$ (the blue solid line) at two distinct points, namely $c = \bar{c}$ and $c = \underline{c}$. Hence, under this scenario, $(c+1/4) > \kappa(c; \gamma)$ if and only if $\underline{c} < c < \bar{c}$. With an increasing γ, the position of $\kappa(c; \gamma)$ shifts towards the up-left direction, and the span on the c-axis between $c = \bar{c}$ and $c = \underline{c}$ shrinks accordingly. At the critical point when $\gamma = \gamma^*$, the straight line $(c + 1/4)$ is tangential to $\kappa(c; \gamma)$ (the black dashed line) and they intersect at a single point $c = c^*$. Ultimately, when $\gamma > \gamma^*$, $\kappa(c; \gamma)$ will never intersect with $(c + 1/4)$ for any values of c. Thus, when $\gamma < \gamma^*$, there always exists a c such that $(c+1/4) > \kappa(c; \gamma)$ stays valid. Using a bisection method, the critical value of the Lipschitz constant is $\gamma^* \approx 1.053$.

5. State estimation for uncertain plant model

In the previous section, a state observer as well as its convergence properties for an uncertainty-free thermal plant model was proposed and analyzed. In this section, the plant model with in-domain and output uncertainties, emerged from the heat generation rate model reduction and temperature measurement noise, is under examination. We employ the same observer structure as in (26)–(29) for the uncertain plant model (14)–(17), and investigate the boundedness of the estimation error in the sense of $\mathcal{L}_2$ norm.

Subtracting (26)–(29) from (14)–(17) produces the observer's error dynamics:

$$\widetilde{T}_t(x, t) = \widetilde{T}_{xx}(x, t) + \phi(x, t) - p_1(x)\widetilde{T}(1, t)$$
$$- p_1(x)\mu(t) + \varepsilon(x, t), \tag{63}$$

$$\widetilde{T}_x(0, t) = 0, \tag{64}$$

$$\widetilde{T}_x(1, t) = -(\delta + p_{10})\widetilde{T}(1, t) - p_{10}\mu(t). \tag{65}$$

The analysis in this scenario is different from the traditional backstepping procedure where the boundary conditions and dynamics are uncertainty-free. It is noteworthy that the system of interest here, (63)–(65), imposes not only a nonlinearity but also modeling uncertainties.

5.1. Backstepping transformation

The backstepping transformation (35) maps the error system (63)–(65) to a target system

$$\omega_t(x, t) = \omega_{xx}(x, t) + \psi(x, t) - c\omega(x, t)$$
$$+ r(x)\mu(t) + \zeta(x, t), \tag{66}$$

$$\omega_x(0, t) = 0, \tag{67}$$

$$\omega_x(1, t) = -(c_1 + \delta)\omega(1, t) - p_{10}\mu(t), \tag{68}$$

where $r(x)$ is an unknown function to be determined and $\psi(x, t)$ satisfies (39). The term $\zeta(x, t)$ is the transformed function from $\varepsilon(x, t)$ by the backstepping transformation with kernel function $K(x, y)$:

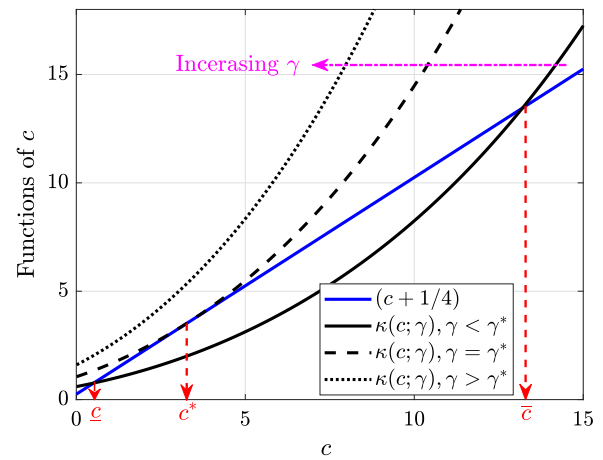$$\varepsilon(x, t) = \zeta(x, t) - \int_x^1 K(x, y)\zeta(y, t)\mathrm{d}y. \tag{69}$$

Fig. 1. An illustration of design parameter selection to guarantee observer convergence. As γ increases, the function $\kappa(c; \gamma)$ shifts towards the upper-left direction and the span between $c = \underline{c}$ and $c = \bar{c}$ shrinks accordingly. When $\gamma < \gamma^* \approx 1.053$, it is ensured that there always exists a design parameter c such that the conditions in (57) hold. (For interpretation of the references to color in this figure legend, the reader is referred to the web version of this article.)

Remark 6. The backstepping transformation (69) for the uncertain terms facilitates the construction of a target system of the form (66)–(68), which is a key enabling step to integrate the in-domain uncertainty into the target system. Moving forward, since $r(x)$ is unknown, the challenge is to determine the functional form of $r(x)$ such that there exists a unique analytic solution to the inverse backstepping transformation kernel function $\ell(x, y)$, and that the target system (66)–(68) is stable.

Similarly, to explicitly determine $K(x, y)$ and $r(x)$, we differentiate both sides of the backstepping transformation (35) with respect to x and t and take into account the target system dynamics (66)–(68). This direct computation leads to (70) which is given in Box I, and note that (70) has to hold for all $(x, t) \in [0, 1] \times [0, \infty)$. Hence, the kernel function $K(x, y)$ exhibits the same structure as that in (40)–(42) from the uncertainty-free case. Moreover, the observer gains also remain unchanged from those in (44) and (45). Finally, in view of the third term in (70), the function $r(x)$ has to verify $\Delta(x) = 0$ with

$$\Delta(x) := r(x) - \int_x^1 K(x, y)r(y)\mathrm{d}y + p_1(x) + p_{10}K(x, 1). \tag{71}$$

The closed-form expression of $r(x)$ will be derived in the forthcoming sections with the aid of the inverse backstepping transformation.

5.2. Inverse backstepping transformation

We adopt the same inverse backstepping transformation (46) which was used for the uncertainty-free case. Differentiating both sides of (46) with respect to x and t produces (72) given in Box I. Again, (72) has to hold for all $(x, t) \in [0, 1] \times [0, \infty)$. Interestingly, in this case, the inverse backstepping kernel $\ell(x, y)$ still satisfies the kernel PDE (47)–(49), whose analytic solution is given by (50). Now, define the following:

$$(\star) := p_1(x) + \ell_y(x, 1) + (\delta + p_{10})\ell(x, 1)$$
$$+ \int_x^1 \ell(x, y)p_1(y)\mathrm{d}y, \tag{73}$$

$$(\star\star) := r(x) + p_1(x) + p_{10}\ell(x, 1) + \int_x^1 \ell(x, y)p_1(y)\mathrm{d}y. \tag{74}$$

$$\int_x^1 \omega(y, t) \left[K_{xx}(x, y) - K_{yy}(x, y) + cK(x, y) \right] dt + \omega(1, t) \left[p_1(x) + K_y(x, 1) + (c_1 + \delta) K(x, 1) \right]$$
$$+ \mu(t) \left[r(x) - \int_x^1 K(x, y)r(y)dy + p_1(x) + p_{10}K(x, 1) \right] - \omega(x, t) \left[2\frac{\partial}{\partial x}K(x, x) + c \right] = 0. \tag{70}$$

$$\int_x^1 \widetilde{T}(y, t) \left[-\ell_{xx}(x, y) + \ell_{yy}(x, y) + c\ell(x, y) \right] dt - \widetilde{T}(1, t) \left[p_1(x) + \ell_y(x, 1) + (\delta + p_{10}) \ell(x, 1) + \int_x^1 \ell(x, y)p_1(y)dy \right]$$
$$- \mu(t) \left[r(x) + p_1(x) + p_{10}\ell(x, 1) + \int_x^1 \ell(x, y)p_1(y)dy \right] - \widetilde{T}(x, t) \left[2\frac{\partial}{\partial x}\ell(x, x) + c \right] = 0. \tag{72}$$

Box I.

Hence, a sufficient condition for (72) to hold for all $(x, t) \in [0, 1] \times [0, \infty)$ is $(\star) = 0$ and $(\star\star) = 0$.

Proposition 4. *Let $(\star)$ and $(\star\star)$ be as in (73) and (74). Then $(\star) = 0$ and $(\star\star) = 0$ for all $x \in [0, 1]$, if and only if*

$$r(x) = \ell_y(x, 1) + \delta\ell(x, 1). \tag{75}$$

We prove Proposition 4 with the assistance of the following Lemma.

Lemma 2. *For $K(x, y)$ and $\ell(x, y)$, which are the kernel functions for the backstepping and the inverse backstepping transformations, it holds from Krstic and Smyshlyaev (2008) and Meurer (2013) that*

$$\ell(x, y) = K(x, y) + \int_x^y K(x, \xi)\ell(\xi, y)d\xi \tag{76}$$

$$= K(x, y) + \int_x^y \ell(x, \xi)K(\xi, y)d\xi. \tag{77}$$

We are now positioned to provide the proof for Proposition 4 utilizing Lemma 2.

Proof. Differentiate both sides of (77) with respect to y, and evaluate at $y = 1$:

$$\ell_y(x, 1) = K_y(x, 1) + \ell(x, 1)K(1, 1) + \int_x^1 \ell(x, \xi)K_y(\xi, 1)d\xi. \tag{78}$$

Next, we substitute $K_y(x, 1)$ and $K(1, 1)$ from (44)–(45) into (78):

$$\ell_y(x, 1) = -p_1(x) - (c_1 + \delta)K(x, 1) + \ell(x, 1)(c_1 - p_{10})$$
$$- \int_x^1 \ell(x, \xi) \left[p_1(\xi) + (c_1 + \delta)K(\xi, 1) \right] d\xi. \tag{79}$$

Re-arranging terms in (79) yields

$$(\star) = -(c_1 + \delta) \left[K(x, 1) - \ell(x, 1) + \int_x^1 \ell(x, \xi)K(\xi, 1)d\xi \right]. \tag{80}$$

In addition, note from (77) that

$$\ell(x, 1) = K(x, 1) + \int_x^1 \ell(x, \xi)K(\xi, 1)d\xi. \tag{81}$$

In view of (80) and (81), we have $(\star) = 0$. Moreover,

$$(\star) - (\star\star) = \ell_y(x, 1) + \delta\ell(x, 1) - r(x). \tag{82}$$

Hence, $(\star\star) = 0$ if and only if $r(x)$ verifies (75). Finally, we must check if the proposed $r(x)$ in (75) satisfies $\Delta(x) = 0$. First, notice from (76) that

$$\ell_y(x, 1) = K_y(x, 1) + \ell(1, 1)K(x, 1) + \int_x^1 K(x, \xi)\ell_y(\xi, 1)d\xi. \tag{83}$$

Substitute $r(x)$ from (75), $p_1(x)$ in (44), and p_{10} from (45), altogether into (71), and we arrives at (84) which is given in Box II, in which the second equality stems from substituting $\ell_y(x, 1)$ using (83), and the last equality is obtained by (76).

5.3. Stability of the target system

The disturbance $\mu(t)$ that appears in the target system via the boundary condition (68) becomes problematic when proving the stability of the target system, due to cross terms involving uncertainty μ and state ω if $\mathcal{L}_2$ norm is employed as the Lyapunov functional candidate. To tackle this issue, we utilize the following invertible transformation $\omega(x, t) \mapsto z(x, t)$ to transfer the boundary uncertainties into the in-domain dynamics:

$$\omega(x, t) = z(x, t) - \frac{1}{2}p_{10}\mu(t)(x^2 - 1). \tag{85}$$

The second term at the right-hand side of (85) is leveraged to cancel the uncertainty term in the boundary condition of the target system. It is also worth noting that this transformation preserves $z(1, t) = \omega(1, t)$. Differentiating the above transformation with respect to x and t yields the dynamics for $z(x, t)$:

$$z_t(x, t) = z_{xx}(x, t) + \psi(x, t) - cz(x, t)$$
$$+ e_\mu(x, t) + \zeta(x, t), \tag{86}$$

where $e_\mu(x, t)$ is a term associated with the uncertainty, given by

$$e_\mu(x, t) = [r(x) - p_{10}]\mu(t) + \frac{p_{10}}{2}(x^2 - 1)[c\mu(t) + \mu_t(t)]. \tag{87}$$

The boundary conditions for $z(x, t)$ is given by

$$z_x(0, t) = \omega_x(0, t) = 0, \tag{88}$$

$$z_x(1, t) = \omega_x(1, t) + p_{10}\mu(t) = -(c_1 + \delta)z(1, t), \tag{89}$$

from which we could observe that the uncertainty μ is no longer at the boundary conditions in the z-system. We provide the estimation error stability in the sense of $\mathcal{L}_2$ norm through the analysis of the transformed system (86)–(89).

Theorem 5 (*Convergence of Robust Observer*). *Consider the observer error dynamics (63)–(65), and let the observer gains $p_1(x)$ and p_{10} be as in (44) and (45). Given Lipschitz constant γ, if the design parameters c and c_1 are selected such that (57) is satisfied, then in the presence of the in-domain uncertainty and the output uncertainty, i.e., $\varepsilon(x, t) \neq 0$ and $\mu(t) \neq 0$, the estimation error remains bounded in the sense of $\mathcal{L}_2$ norm denoted by $\left\| \widetilde{T}(\cdot, t) \right\| \leq R_B(c, c_1)$ as $t \to \infty$, where*

$$R_B(c, c_1) := [1 + \eta(c)] \cdot \left[\frac{\beta(c, c_1)}{\alpha(c)} + \lambda(c, c_1) \right]. \tag{90}$$

$$\Delta(x) = \ell_y(x, 1) + \delta\ell(x, 1) - K_y(x, 1) - (c_1 + \delta)K(x, 1) + \left(c_1 + \frac{c}{2}\right)K(x, 1) - \int_x^1 K(x, \xi)\left[\ell_y(\xi, 1) + \delta\ell(\xi, 1)\right]\mathrm{d}\xi$$

$$= \delta\left[\ell(x, 1) - K(x, 1) - \int_x^1 K(x, \xi)\ell(\xi, 1)\mathrm{d}\xi\right] \equiv 0. \tag{84}$$

Box II.

Specifically,

$$\alpha(c) := c - \kappa(c; \gamma) + \frac{1}{4}, \tag{91}$$

$$\beta(c, c_1) := \kappa(c; \gamma)\lambda(c, c_1) + \|r(x) - p_{10}\|\overline{\mu}$$
$$+ \sqrt{\frac{2}{15}}|p_{10}|\overline{U} + (1 + \rho(c))\overline{\varepsilon}, \tag{92}$$

$$\lambda(c, c_1) := \sqrt{\frac{2}{15}}|p_{10}|\overline{\mu}, \tag{93}$$

where $\overline{U} = \max_t\{c\mu(t) + \dot{\mu}(t)\}$.

Proof. Consider the Lyapunov functional candidate,

$$W_2(t) = \frac{1}{2}\int_0^1 z^2(x, t)\mathrm{d}x = \frac{1}{2}\|z(x, t)\|^2. \tag{94}$$

The time derivative of the Lyapunov function $W_2(t)$ along the trajectory of $z(x, t)$ can be computed as

$$\dot{W}_2(t) = \int_0^1 z(x, t)z_t(x, t)\mathrm{d}x$$
$$= \int_0^1 zz_{xx}\mathrm{d}x + \int_0^1 z\psi\,\mathrm{d}x - c\int_0^1 z^2\mathrm{d}x$$
$$+ \int_0^1 ze_\mu\mathrm{d}x + \int_0^1 z\zeta\,\mathrm{d}x. \tag{95}$$

Applying the integration by parts to the first term, and Cauchy–Schwarz inequality to the second, fourth, fifth, and sixth term at the right-hand side of (95) results in

$$\dot{W}_2(t) \leq -(c_1 + \delta)z^2(1) - \|z_x\|^2 - c\|z\|^2$$
$$+ (\|\psi\| + \|e_\mu\| + \|\zeta\|)\|z\|. \tag{96}$$

Now consider the transformation (85) and apply triangular inequality to conclude

$$\|\omega\| \leq \|z\| + \frac{1}{2}\|p_{10}\mu(t)(1 - x^2)\| \leq \|z\| + \lambda(c, c_1), \tag{97}$$

so that the upper bound of $\|\psi\|$ given by (51) is explicitly expressed in terms of state in z system:

$$\|\psi\| \leq \kappa(c; \gamma)\|z\| + \kappa(c; \gamma)\lambda(c, c_1). \tag{98}$$

Furthermore, from (87), the following upper bound is imposed on e_μ,

$$\|e_\mu\| \leq \|r(x) - p_{10}\|\overline{\mu} + \sqrt{\frac{2}{15}}|p_{10}|\overline{U}. \tag{99}$$

Finally, by recognizing the inverse backstepping transformation $\zeta(x, t) \mapsto \varepsilon(x, t)$,

$$\zeta(x, t) = \varepsilon(x, t) + \int_x^1 \varepsilon(y, t)\ell(x, y)\mathrm{d}y, \tag{100}$$

similar strategy as that in Lemma 1 and (55) can be employed to derive an upper bound on $\|\zeta(\cdot, t)\|$:

$$\|\zeta(\cdot, t)\| \leq [1 + \rho(c)]\overline{\varepsilon}. \tag{101}$$

Substituting (97)–(99) and (101) into the right-hand side of (96), and applying the Poincaré inequality, $-\|z_x\|^2 \leq \frac{1}{2}z^2(1) - \frac{1}{4}\|z\|^2$, to the second term on the right-hand side of (96), yields

$$\dot{W}_2 \leq -\left(c_1 + \delta - \frac{1}{2}\right)z^2(1) - \alpha(c)\|z\|^2 + \beta(c, c_1)\|z\|. \tag{102}$$

If c_1 is chosen such that $c_1 \geq 1/2 - \delta$ and $\alpha(c) > 0$, or equivalently $c > \kappa(c; \gamma) - 1/4$, the comparison principle (Khalil, 1996) applied to (102) gives

$$\|z(\cdot, t)\| \leq \frac{\beta(c, c_1)}{\alpha(c)} + \left[\|z(\cdot, 0)\| - \frac{\beta(c, c_1)}{\alpha(c)}\right]e^{-\alpha(c)t}. \tag{103}$$

Since the inverse transformation $z(x, t) \mapsto \omega(x, t)$ is unique,

$$z(x, t) = \omega(x, t) + \frac{1}{2}p_{10}\mu(t)(x^2 - 1), \tag{104}$$

and the backstepping transformation (35) is invertible, an upper bound of $\|\widetilde{T}(\cdot, t)\|$ is computed via the sequence of inequalities leveraging (56) and (97):

$$\|\widetilde{T}(\cdot, t)\| \leq [1 + \eta(c)] \cdot [\|z(\cdot, t)\| + \lambda(c, c_1)]. \tag{105}$$

When $t \to \infty$, the exponential terms at the right-hand side of (105) decays to zero. Under this scenario,

$$\|\widetilde{T}(\cdot, t)\| \leq [1 + \eta(c)] \cdot \left[\frac{\beta(c, c_1)}{\alpha(c)} + \lambda(c, c_1)\right]. \tag{106}$$

This completes the proof.

Remark 7. The estimation error bound R_B is characterized by the observer gains, Lipschitz constant, and bounds on the uncertainties. For a given Lipschitz constant $\gamma < \gamma^*$, one can minimize the size of the error ball R_B to achieve robust estimation by formulating and solving the optimization problem

$$\min_{c, c_1} \quad R_B(c, c_1)$$
$$\text{s.t.} \quad \kappa(c; \gamma) - c - \frac{1}{4} < 0$$
$$- c_1 + \frac{1}{2} - \delta \leq 0 \tag{107}$$
$$c > 0$$

6. Simulation studies

In this section, we present simulation studies to demonstrate the performance of the proposed thermal observer on a commercial Lithium-Iron Phosphate (LFP) A123 26650 cylindrical cell with rated capacity of 2.3 Ah. In this study, the one-dimensional thermal model (14)–(18) is used as the plant model. The model parameters have been previously identified in Dey et al. (2019) and Liao, Zuo, Ma, Chen, An, Gao, and Yin (2012) using experimental data, and are enumerated in Table 1. The calculation leveraging the formula in (20) using these parameters yields $\gamma = 0.0072 |I|_{\max}^2$. Hence, the analysis in Section 4 indicates that, to guarantee the sufficient conditions of observer convergence, the absolute maximum value of the applied current is $|I|_{\max}$

Table 1
Model Parameters for a commercial LFP A123 26650 cylindrical Cell.

Symbols	Values	Units
T_{ref}	298.15	K
T_{amb}	298.15	K
$R_{s,\text{ref}}$	15	mΩ
E_a	33.8	kJ/mol
k	0.61	W/(m K)
h	69.89	W/(m^2 K)
R	8.314	J/(mol K)
D	2118	kg/m^3
c_p	711	J/(kg K)
C_{batt}	2.26	Ah
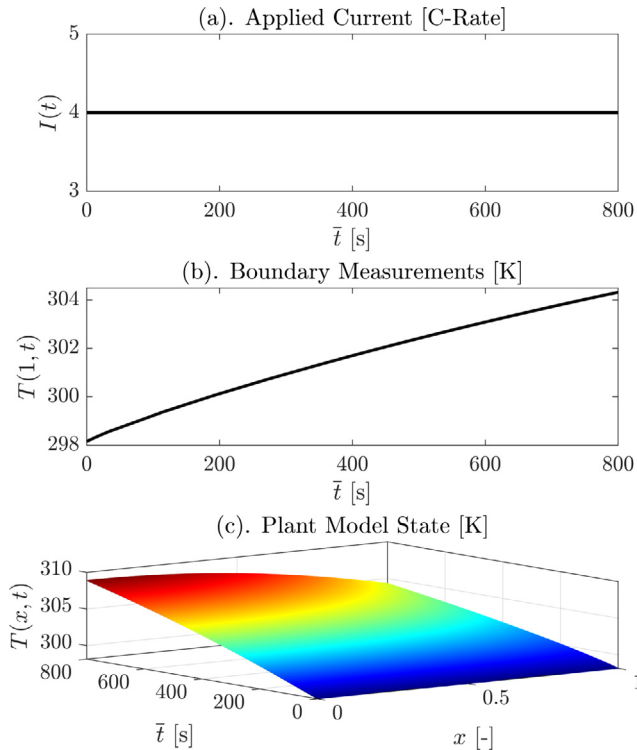
Fig. 2. The plant model response under a 4C constant current. Plant model initial condition: $T_0(x) = T_{\text{amb}} = 298.15$ K for all $x \in [0, 1]$.

$= \sqrt{\gamma^*/0.0072} \approx 12$A (equivalently 5.4C). This current rate is generally well beyond the operating current limits of a cylindrical LFP cell — reaffirming the applicability of the proposed observer even under extreme practical conditions. Let the premises in Assumption 1 hold, we evaluate the effectiveness of the observer with and without the presence of in-domain and output uncertainties. For the purpose of demonstrating the estimation results, the state estimates are initialized with incorrect values to imitate uncertainty in initial conditions. Furthermore, we quantify the performance of the observers in terms of $\mathcal{L}_2$ estimation error convergence time, defined as the time spent to reach within ± 0.2 K band of zero starting from a non-zero initial condition.

6.1. No in-domain and output uncertainties

We first encapsulate the performance of the proposed temperature estimation approach under no uncertainties, i.e., $\varepsilon(x, t) = 0$ and $\mu(t) = 0$, $\forall (x, t) \in [0, 1] \times [0, \infty)$. A 4C constant current, shown in Fig. 2(a), is applied to the plant model to generate battery thermal responses. The simulation time is $\bar{t} \in [0, 800 \text{ s}]$, and the spatial domain is $r \in [0, 0.013 \text{ m}]$, i.e., $x \in [0, 1]$. The finite
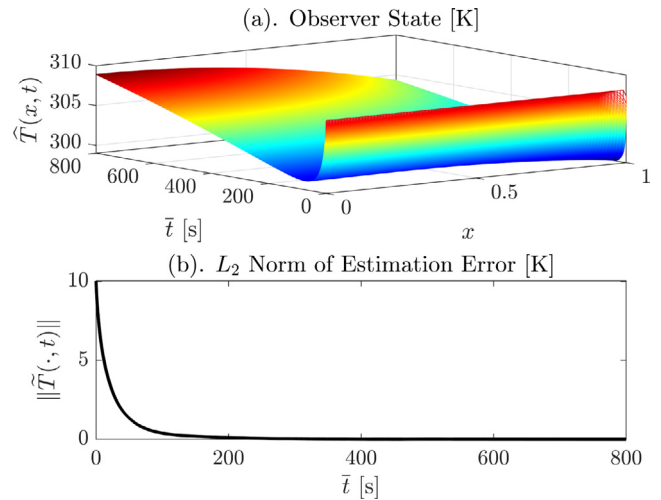
Fig. 3. Observer results for a 4C constant current. Observer initial condition: $\widehat{T}(x, 0) = T_0(x) + 10$ K for all $x \in [0, 1]$. The estimation error converges to zero exponentially in the sense of $\mathcal{L}_2$ spatial norm, thus confirming the conclusion from Theorem 3.

difference method is employed to numerically discretize the plant model. More precisely, the plant model is discretized spatially with 100 grid points. The left and right boundary conditions are handled by the second-order forward and backward approximations, respectively. The simulation is numerically implemented in MATLAB®. Suppose the battery cell has been in resting prior to the simulation onset such that the initial condition of the plant model is uniformly set to the ambient temperature, i.e., $T_0(x) = T_{\text{amb}} = 298.15$ K for all $x \in [0, 1]$. As such, the measured boundary signals and the spatially distributed temperature profile are sketched in Fig. 2(b) and Fig. 2(c), respectively. Further, the absolute maximum current in this specific case is $|I|_{\max} = 4$C. With this, the expression in (20) provides the numerical value of the Lipschitz constant for the nonlinearity function f with respect to T in the plant model, i.e., $\gamma = 0.59 < \gamma^*$. This guarantees the existence of a design parameter c such that the observer convergence conditions presented in Theorem 3 are fulfilled. In fact, the feasible ranges for the design parameters in this case are $0.49 < c < 13.5$ and $c_1 \geq -0.53$. With the choice of $c = 8$ and $c_1 = 2$, the in-domain observer gain $p_1(x)$ and the boundary observer gain p_{10} can be computed with the assistance of backstepping kernels as well as (44) and (45). Ultimately, Fig. 3(a) presents the observer state, whereas Fig. 3(b) shows exponential convergence of $\mathcal{L}_2$ norm of temperature estimation error to zero, despite incorrect initial conditions ($\widehat{T}_0(x) = T_0(x) + 10$ K for all $x \in [0, 1]$). The estimates $\widehat{T}$ converge to the true value T within 100 s. The numerical simulation results confirm our analysis in Theorem 3. It additionally demonstrates promising estimation performance under high-rate operating modes which are suitable for various battery fast charging applications.

Next, we apply an electric vehicle charge/discharge cycle. This input current profile shown in Fig. 4(a) is generated from concatenating two Federal Urban Driving Schedule (FUDS) drive cycles referenced in Xing, He, Pecht, and Tsui (2014). The absolute maximum C-rate is scaled to 5.3C — confirming the existence of a design parameter c such that the observer convergence conditions in Theorem 3 are verified. From a simple computation, this current profile would roughly cause 50.1% change in battery SOC. In particular, the boundary measurements and temperature responses are plotted in Fig. 4(b) and Fig. 4(c). It can be observed that this dynamic current profile produces less aggressive temperature variations across spatial and temporal domains. This
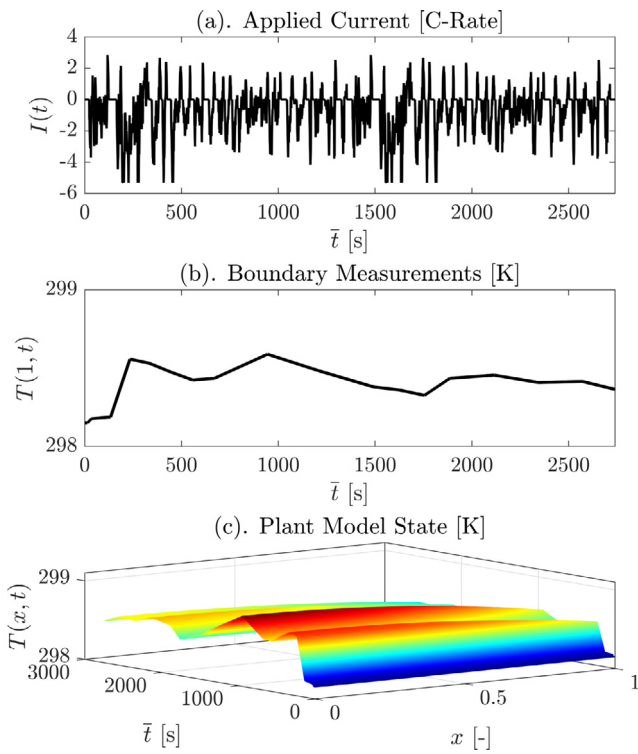
Fig. 4. The plant model response under a FUDS drive cycle. Plant model initial condition: $T_0(x) = T_{amb} = 298.15$ K for all $x \in [0, 1]$.
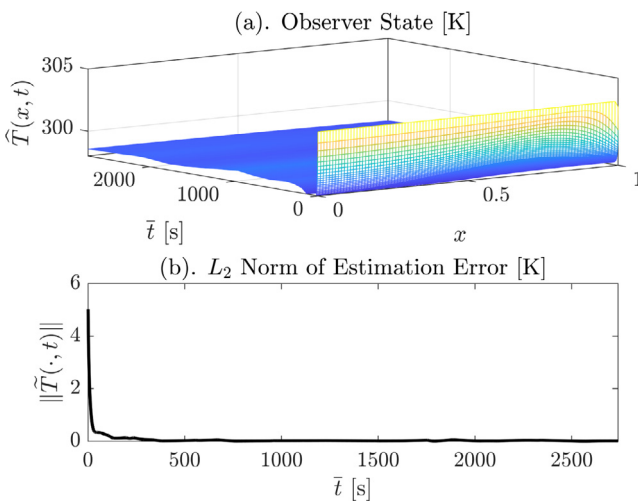

Fig. 5. Observer results for a FUDS drive cycle. Observer initial condition: $\widehat{T}(x, 0) = T_0(x) + 5$ K for all $x \in [0, 1]$. The estimation error converges to zero exponentially within 120 s in the sense of $\mathcal{L}_2$ norm.

is because unlike the high-rate constant current input from the previous study, this dynamic cycle is characterized mostly by non-sustained C-rates. To further emulate real-world scenarios and evaluate the observer's robustness with respect to parametric uncertainty in the surface heat transfer coefficient h, we inject 10% error in parameter h used in the observer simulation. Consequently, regardless of an incorrect initialization, the observer converges exponentially in the sense of $\mathcal{L}_2$ norm after the initial transient ($\sim$110 s), as visualized in Fig. 5(b). Moreover, the simulation reported in Fig. 5 demonstrates no apparent estimation bias from the uncertainty in parameter h, highlighting the observer's robustness against the imperfection in h values.
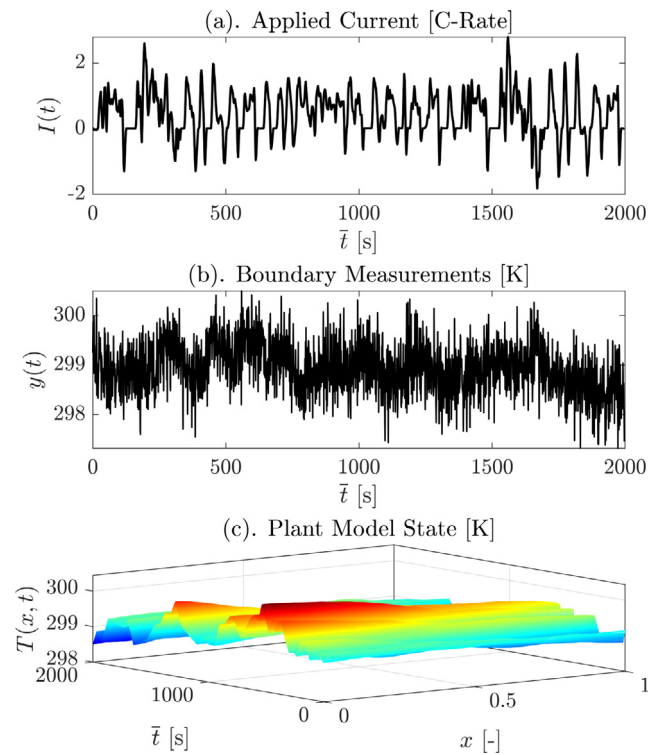

Fig. 6. The plant model response under a UDDS drive cycle. Plant model initial condition: $T_0(x) = T_{amb} + 1$ K $= 299.15$ K for all $x \in [0, 1]$. Gaussian noise with 0.3 K variance and zero mean, i.e., $\mu(t) \sim \mathcal{N}(0, 1)$, is injected to the boundary measurement signal $y(t)$. Uniformly distributed random noise $\varepsilon(x, t)$ is introduced into the plant model (14).

6.2. With in-domain and output uncertainties

Finally, we demonstrate simulation results for the robust observer acting on the plant model with uncertainties. Gaussian noises with 0.3 K variance and zero mean, i.e., $\mu(t) \sim \mathcal{N}(0, 0.3)$, is manually injected to the boundary measurement signal $T(1, t)$ (see Eq. (18)). Further, a uniformly distributed random noise $\varepsilon(x, t)$ is introduced to the plant model (14). The trajectory of the applied current, which is extracted from the Urban Dynamometer Driving Schedule (UDDS) driving cycle, is shown in Fig. 6(a). The choice of UDDS is to imitate a practical electric vehicle driving pattern. The noise-corrupted boundary measurement $y(t)$ and the spatially distributed temperature profile $T(x, t)$ are plotted in Fig. 6(b) and Fig. 6(c), respectively. Notice that the same observer gains $p_1(x)$ and p_{10} as those from the uncertainty-free case are utilized. Once again, the observer is initialized uniformly to an incorrect value, and the $\mathcal{L}_2$ norm of the estimation error quickly converges to a ball of radius R_B around the equilibrium point $\|\widetilde{T}\| = 0$, as can be seen in Fig. 7(b). Recall that Theorem 5 only guarantees boundedness of estimation error, in the sense of $\mathcal{L}_2$ norm. These results are generated by setting $c = 0.5$ and $c_1 = 1/2 - \delta = -0.99$, and the numerical value of $R_B(c, c_1)$ computed by (90) is also provided in Fig. 7(b) to illustrate the effectiveness of the derived estimation error bounds. Notably, the convergence time is within 540 s, whereas R_B tightly bounds the estimation error for all $t \geq 390$ s. The enabling step for the proposed robust observer approach is to solve the nonlinear optimization problem in Remark 7 to minimize the magnitude of R_B. Herein, it is also highlighted that R_B expands monotonically with respect to parameter c, whereas the observer convergence rate becomes faster as c increases. There is then a trade-off between observer convergence rate and the allowable magnitude
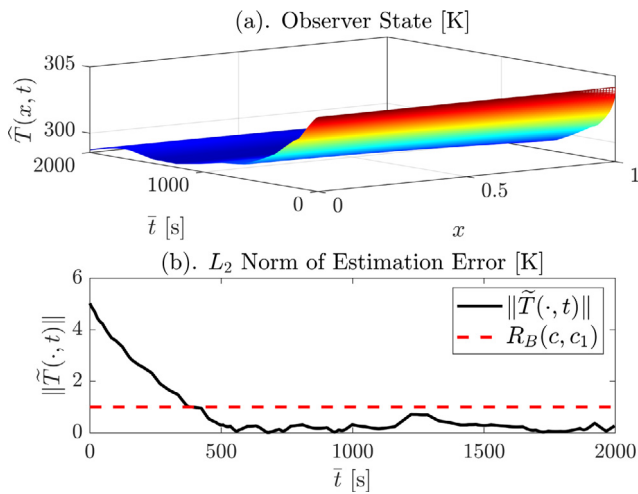
Fig. 7. Observer results for a UDDS cycle, subject to in-domain and output uncertainties. Observer initial condition: $\widehat{T}(x, 0) = T_0(x) + 5$ K for all $x \in [0, 1]$. The estimation error converges to a ball of radius R_B around the equilibrium point $\widetilde{T} = 0$ in the sense of $\mathcal{L}_2$ norm, thus justifying the conclusion from Theorem 5.

of R_B. The choice of parameter c for this simulation study was carefully calibrated such that convergence rate and derived error bound simultaneously remain reasonable.

7. Conclusion and future works

The knowledge of real-time battery internal temperature information enables safe and reliable operations. In this regard, an infinite-dimensional PDE boundary observer is proposed for a one-dimensional battery thermal model subject to in-domain and output uncertainties. The estimation error system is converted to a prescribed stable target system, from which the exponential stability of the error dynamics is mathematically derived without the presence of system uncertainties, thanks to the Lipschitz continuous nonlinearity. In the presence of system uncertainties, we transfer the bounded uncertainties in the boundary conditions of the target system into the in-domain dynamics, and the corresponding estimation error converges to an error ball around the equilibrium point, which can be explicitly characterized by uncertainty bounds, observer parameters, and model parameters.

This scheme is regarded as a leap forward in the effort to design estimation algorithms for battery high-fidelity thermal models, without relying on prior spatial discretization of the PDEs. It is also one of the first to simultaneously consider PDE model nonlinearity, modeling uncertainty, and measurement uncertainty within a single observer design framework.

Certain model reductions are made in this study, and their relaxation incentivizes future research directions. This includes extending the proposed estimation algorithm to high-dimensional thermal PDE models, and exploring less conservative necessary and sufficient conditions to ensure observer's exponential convergence. One could also consider coupling thermal effects with battery electrochemical models (Zhang, Couto, & Moura, 2020a). Besides, optimal thermal control and sensor placement could be explored in battery packs (Couto, Zhang, Aitio, Moura, & Howey, 2020).

References

Ahmed-Ali, Tarek, Giri, Fouad, Krstic, Miroslav, Burlion, Laurent, & Lamnabhi-Lagarrigue, Françoise (2016). Adaptive boundary observer for parabolic PDEs subject to domain and boundary parameter uncertainties. *Automatica*, 72, 115–122.

Al Hallaj, Said, Maleki, Hossein, Hong, Jong-Sung, & Selman, J. Robert (1999). Thermal modeling and design considerations of lithium-ion batteries. *Journal of Power Sources*, 83(1–2), 1–8.

Bernardi, D., Pawlikowski, E., & Newman, John (1985). A general energy balance for battery systems. *Journal of The Electrochemical Society*, 132(1), 5–12.

Broussely, Michel, Biensan, Ph, Bonhomme, F., Blanchard, Ph, Herreyre, S., Nechev, K., et al. (2005). Main aging mechanisms in Li ion batteries. *Journal of Power Sources*, 146(1–2), 90–96.

Chaturvedi, Nalin A., Klein, Reinhardt, Christensen, Jake, Ahmed, Jasim, & Kojic, Aleksandar (2010). Algorithms for advanced battery-management systems. *IEEE Control Systems Magazine*, 30(3), 49–68.

Chen, S. C., Wan, C. C., & Wang, Y. Y. (2005). Thermal analysis of lithium-ion batteries. *Journal of Power Sources*, 140(1), 111–124.

Cheng, Meng-Bi, Radisavljevic, Verica, & Su, Wu-Chung (2011). Sliding mode boundary control of a parabolic PDE system with parameter variations and boundary uncertainties. *Automatica*, 47(2), 381–387.

Couto, Luis D., Zhang, Dong, Aitio, Antti, Moura, Scott, & Howey, David (2020). Estimation of parameter probability distributions for lithium-ion battery string models using Bayesian methods. In *Dynamic systems and control conference, (Vol. 84270)*. American Society of Mechanical Engineers, V001T20A003.

Dey, Satadru, Ayalew, Beshah, & Pisu, Pierluigi (2015). Nonlinear robust observers for state-of-charge estimation of lithium-ion cells based on a reduced electrochemical model. *IEEE Transactions on Control Systems Technology*, 23(5), 1935–1942.

Dey, Satadru, Biron, Zoleikha Abdollahi, Tatipamula, Sagar, Das, Nabarun, Mohon, Sara, Ayalew, Beshah, et al. (2016). Model-based real-time thermal fault diagnosis of lithium-ion batteries. *Control Engineering Practice*, 56, 37–48.

Dey, S., Perez, H. E., & Moura, S. J. (2019). Model-based battery thermal fault diagnostics: Algorithms, analysis, and experiments. *IEEE Transactions on Control Systems Technology*, [ISSN: 1063-6536] 27(2), 576–587. http://dx.doi.org/10.1109/TCST.2017.2776218.

Doughty, Daniel H., Butler, Paul C., Jungst, Rudolph G., & Roth, E. Peter (2002). Lithium battery thermal models. *Journal of Power Sources*, 110(2), 357–363.

Du, Ronghua, Hu, Xiaosong, Xie, Shaobo, Hu, Lin, Zhang, Zhiyong, & Lin, Xianke (2020). Battery aging-and temperature-aware predictive energy management for hybrid electric vehicles. *Journal of Power Sources*, 473, Article 228568.

Evans, T. I., & White, Ralph E. (1989). A thermal analysis of a spirally wound battery using a simple mathematical model. *Journal of The Electrochemical Society*, 136(8), 2145.

Forgez, Christophe, Do, Dinh Vinh, Friedrich, Guy, Morcrette, Mathieu, & Delacourt, Charles (2010). Thermal modeling of a cylindrical LiFePO$_4$/graphite lithium-ion battery. *Journal of Power Sources*, 195(9), 2961–2968.

Gu, W. B., & Wang, Chao-Yang Thermal and electrochemical coupled modeling of a lithium-ion cell. In *Proceedings of the ECS, (Vol. 99)* (pp. 748–762).

Hu, Y., & Yurkovich, S. (2012). Battery cell state-of-charge estimation using linear parameter varying system techniques. *Journal of Power Sources*, 198, 338–350.

Käbitz, Stefan, Gerschler, Jochen Bernhard, Ecker, Madeleine, Yurdagel, Yusuf, Emmermacher, Brita, André, Dave, et al. (2013). Cycle and calendar life study of a graphite | LiNi$_{1/3}$mn$_{1/3}$co$_{1/3}$o$_2$ Li-ion high energy system. Part A: Full cell characterization. *Journal of Power Sources*, 239, 572–583.

Keyser, Matthew, Pesaran, Ahmad, Li, Qibo, Santhanagopalan, Shriram, Smith, Kandler, Wood, Eric, et al. (2017). Enabling fast charging–battery thermal considerations. *Journal of Power Sources*, 367, 228–236.

Khalil, Hassan K. (1996). *Noninear systems, (Vol. 2)*. (5), New Jersey: Prentice-Hall, 5–1.

Kim, Youngki, Mohan, Shankar, Siegel, Jason B., Stefanopoulou, Anna G., & Ding, Yi (2014). The estimation of temperature distribution in cylindrical battery cells under unknown cooling conditions. *IEEE Transactions on Control Systems Technology*, 22(6), 2277–2286.

Kim, Gi-Heon, Pesaran, Ahmad, & Spotnitz, Robert (2007). A three-dimensional thermal abuse model for lithium-ion cells. *Journal of Power Sources*, 170(2), 476–489.

Kim, Hahnsang, & Shin, Kang G. (2011). Efficient sensing matters a lot for large-scale batteries. In *2011 IEEE/ACM second international conference on cyber-physical systems* (pp. 197–205). IEEE.

Klein, Reinhardt, Chaturvedi, Nalin A., Christensen, Jake, Ahmed, Jasim, Findeisen, Rolf, & Kojic, Aleksandar (2013). Electrochemical model based observer design for a lithium-ion battery. *IEEE Transactions on Control Systems Technology*, 21(2), 289–301.

Koniak, M., & Czerepicki, A. (2017). Selection of the battery pack parameters for an electric vehicle based on performance requirements. In *IOP conference series: Materials science and engineering, (Vol. 211)*. IOP Publishing, Article 012005.

Krstic, Miroslav (1999). On global stabilization of Burgers' equation by boundary control. *Systems & Control Letters*, 37(3), 123–141.

Krstic, Miroslav, & Smyshlyaev, Andrey (2008). *Boundary control of PDEs: A course on backstepping designs, (Vol. 16)*. Siam.

Liao, Lixia, Zuo, Pengjian, Ma, Yulin, Chen, XinQun, An, Yongxin, Gao, Yunzhi, et al. (2012). Effects of temperature on charge/discharge behaviors of LiFePO$_4$ cathode for Li-ion batteries. *Electrochimica Acta*, 60, 269–273.

Liaw, Bor Yann, Roth, E. Peter, Jungst, Rudolph G., Nagasubramanian, Ganesan, Case, Herbert L., & Doughty, Daniel H. (2003). Correlation of arrhenius behaviors in power and capacity fades with cell impedance and heat generation in cylindrical lithium-ion cells. *Journal of Power Sources*, 119, 874–886.

Lin, Xinfan, Perez, Hector E., Mohan, Shankar, Siegel, Jason B., Stefanopoulou, Anna G., Ding, Yi, et al. (2014). A lumped-parameter electro-thermal model for cylindrical batteries. *Journal of Power Sources*, 257, 1–11.

Lin, Xinfan, Perez, Hector E., Siegel, Jason B., Stefanopoulou, Anna G., Li, Yonghua, Anderson, R. Dyche, et al. (2013). Online parameterization of lumped thermal dynamics in cylindrical lithium ion batteries for core temperature estimation and health monitoring. *IEEE Transactions on Control Systems Technology*, 21(5), 1745–1755.

Meurer, Thomas (2013). On the extended luenberger-type observer for semilinear distributed-parameter systems. *IEEE Transactions on Automatic Control*, 58(7), 1732–1743.

Moura, Scott J., Argomedo, Federico Bribiesca, Klein, Reinhardt, Mirtabatabaei, Anahita, & Krstic, Miroslav (2017). Battery state estimation for a single particle model with electrolyte dynamics. *IEEE Transactions on Control Systems Technology*, 25(2), 453–468.

Muratori, Matteo, Canova, Marcello, & Guezennec, Yann (2012). A spatially-reduced dynamic model for the thermal characterisation of Li-ion battery cells. *International Journal of Vehicle Design*, 58(2), 134.

Nambu, Takao (1984). On the stabilization of diffusion equations: boundary observation and feedback. *Journal of Differential Equations*, 52(2), 204–233.

Park, Chanwoo, & Jaura, Arun K. (2003). *Dynamic thermal model of Li-ion battery for predictive behavior in hybrid and fuel cell vehicles*: Technical report, SAE Technical Paper.

Pazy, Amnon (2012). *Semigroups of linear operators and applications to partial differential equations, (Vol. 44)*. Springer Science & Business Media.

Plett, Gregory L. (2004). Extended Kalman filtering for battery management systems of LiPB-based HEV battery packs: Part 3. State and parameter estimation. *Journal of Power Sources*, 134(2), 277–292.

Rajamani, Rajesh (1998). Observers for Lipschitz nonlinear systems. *IEEE Transactions on Automatic Control*, 43(3), 397–401.

Richardson, Robert R., Ireland, Peter T., & Howey, David A. (2014). Battery internal temperature estimation by combined impedance and surface temperature measurement. *Journal of Power Sources*, 265, 254–261.

Samad, Nassim A., Siegel, Jason B., & Stefanopoulou, Anna G. (2014). Parameterization and validation of a distributed coupled electro-thermal model for prismatic cells. In *Dynamic systems and control conference, (Vol. 46193)*. American Society of Mechanical Engineers, V002T23A006.

Smith, Kandler, & Wang, Chao-Yang (2006). Power and thermal characterization of a lithium-ion battery pack for hybrid-electric vehicles. *Journal of Power Sources*, 160(1), 662–673.

Smyshlyaev, Andrey, & Krstic, Miroslav (2005). On control design for PDEs with space-dependent diffusivity or time-dependent reactivity. *Automatica*, 41(9), 1601–1608.

Smyshlyaev, Andrey, & Krstic, Miroslav (2010). *Adaptive control of parabolic PDEs*. Princeton University Press.

Song, Li, & Evans, James W. (2000). Electrochemical-thermal model of lithium polymer batteries. *Journal of The Electrochemical Society*, 147(6), 2086–2095.

Tang, Shu-Xia, Camacho-Solorio, Leobardo, Wang, Yebin, & Krstic, Miroslav (2017). State-of-charge estimation from a thermal–electrochemical model of lithium-ion batteries. *Automatica*, 83, 206–219.

Thomas, Karen E., & Newman, John (2003). Thermal modeling of porous insertion electrodes. *Journal of The Electrochemical Society*, 150(2), A176.

Tranter, Thomas George, Timms, Robert, Shearing, Paul R., & Brett, Dan (2020). Communication—-Prediction of thermal issues for larger format 4680 cylindrical cells and their mitigation with enhanced current collection. *Journal of The Electrochemical Society*.

Vazquez, Rafael, & Krstic, Miroslav (2008a). Control of 1-D parabolic PDEs with Volterra nonlinearities, Part I: design. *Automatica*, 44(11), 2778–2790.

Vazquez, Rafael, & Krstic, Miroslav (2008b). Control of 1D parabolic PDEs with Volterra nonlinearities, Part II: analysis. *Automatica*, 44(11), 2791–2803.

Wang, John, Liu, Ping, Hicks-Garner, Jocelyn, Sherman, Elena, Soukiazian, Souren, Verbrugge, Mark, et al. (2011). Cycle-life model for graphite-LiFePO$_4$ cells. *Journal of Power Sources*, 196(8), 3942–3948.

Wang, Qingsong, Ping, Ping, Zhao, Xuejuan, Chu, Guanquan, Sun, Jinhua, & Chen, Chunhua (2012). Thermal runaway caused fire and explosion of lithium ion battery. *Journal of Power Sources*, 208, 210–224.

Xing, Yinjiao, He, Wei, Pecht, Michael, & Tsui, Kwok Leung (2014). State of charge estimation of lithium-ion batteries using the open-circuit voltage at various ambient temperatures. *Applied Energy*, 113, 106–115.

Yang, Xiao-Guang, Liu, Teng, & Wang, Chao-Yang (2021). Thermally modulated lithium iron phosphate batteries for mass-market electric vehicles. *Nature Energy*, 1–10.

Zhang, Dong, Couto, Luis D., & Moura, Scott J. (2020a). Electrode-level state estimation in lithium-ion batteries via Kalman decomposition. *IEEE Control Systems Letters*, 5(5), 1657–1662.

Zhang, Dong, Couto, Luis D., Park, Saehong, Gill, Preet, & Moura, Scott J. (2020b). Nonlinear state and parameter estimation for li-ion batteries with thermal coupling. *IFAC-PapersOnLine*, 53(2), 12479–12484.

Zhang, Dong, Dey, Satadru, Couto, Luis D., & Moura, Scott J. (2019a). Battery adaptive observer for a single-particle model with intercalation-induced stress. *IEEE Transactions on Control Systems Technology*.

Zhang, Dong, Dey, Satadru, Perez, Hector E., & Moura, Scott J. (2017). Remaining useful life estimation of lithium-ion batteries based on thermal dynamics. In *2017 American control conference* (pp. 4042–4047). IEEE.

Zhang, Dong, Dey, Satadru, Perez, Hector E., & Moura, Scott J. (2019b). Real-time capacity estimation of lithium-ion batteries utilizing thermal dynamics. *IEEE Transactions on Control Systems Technology*.

Zhang, Dong, Tang, Shu-Xia, & Moura, Scott J. (2019c). State and disturbance estimator for unstable reaction-advection-diffusion PDE with boundary disturbance. In *2019 Proceedings of the conference on control and its applications* (pp. 67–74). SIAM.

Dong Zhang received his Ph.D. and M.S. degrees from the University of California at Berkeley, Berkeley, CA, USA, in 2020 and 2016, respectively, all in systems and control engineering. He also earned his B.S. degree from the University of Michigan, Ann Arbor, MI, USA, in 2015, in Civil and Environmental Engineering. He was also awarded a double B.S. degree in Electrical and Computer Engineering from Shanghai Jiao Tong University, Shanghai, China, in 2015. He is currently a Postdoctoral Research Associate with the Department of Mechanical Engineering at Carnegie Mellon University, Pittsburgh, PA, USA. His current research interests include dynamical system estimation and controls, optimization, machine learning, renewable energy systems, energy storage, and advanced Lithium-Ion battery management systems. Dr. Zhang is a recipient of the American Society of Mechanical Engineers (ASME) Energy System Best Paper Award and Finalist at 2020 American Control Conference (ACC) and 2020 Dynamic Systems and Control Conference (DSCC).

Satadru Dey received the master's degree in control systems from IIT Kharagpur, India, in 2010, and the Ph.D. degree in automotive engineering from Clemson University in 2015. From 2015 to 2017, he was a Post-Doctoral Researcher with the University of California at Berkeley, Berkeley. From August 2017 to August 2020, he was an Assistant Professor with the University of Colorado Denver. He is currently an Assistant Professor with the Department of Mechanical Engineering, The Pennsylvania State University. His current research interests include controls, smart cities, energy, and transportation systems.

Shu-Xia Tang received her Ph.D. in Mechanical Engineering in 2016 from the Department of Mechanical & Aerospace Engineering, University of California, San Diego, USA. She is currently an assistant professor at the Department of Mechanical Engineering, Texas Tech University, USA. She is an IEEE senior member and is an IEEE CSS (Control Systems Society) Technical Committee member on Distributed Parameter Systems. She serves as an associate editor of Journal of Control, Automation and Electrical Systems and as an Editorial Board member of IEEE CSS and ASME DSCC (Dynamic Systems and Control Division). Her main research interests are stability analysis, estimation and control design of distributed parameter systems.

Ross Drummond received a D.Phil. in control engineering from the University of Oxford, U.K (2013–2017) where he is currently a UKIC research fellow in the Control Group. His main research interests include the stability analysis of nonlinear feedback systems which he combines with more applied research on the modeling and design of electrochemical energy storage devices, including Li-ion batteries and supercapacitors.

Scott J. Moura is an Associate Professor in Civil and Environmental Engineering and Director of the Energy, Controls, & Applications Lab (eCAL) at the University of California, Berkeley. He is also a faculty member at the Tsinghua-Berkeley Shenzhen Institute. He received the B.S. degree from the University of California, Berkeley, CA, USA, and the M.S. and Ph.D. degrees from the University of Michigan, Ann Arbor, in 2006, 2008, and 2011, respectively, all in mechanical engineering. From 2011 to 2013, he was a Post-Doctoral Fellow at the Cymer Center for Control Systems and Dynamics, University of California, San Diego. In 2013, he was a Visiting Researcher at the Centre Automatique et Systémes, MINES ParisTech, Paris, France. His research interests include control, optimization, and machine learning for batteries, electrified vehicles, and distributed energy resources.

Dr. Moura is a recipient of the National Science Foundation (NSF) CAREER Award, Carol D. Soc Distinguished Graduate Student Mentor Award, the Hellman Fellowship, the O. Hugo Shuck Best Paper Award, the ACC Best Student Paper Award (as advisor), the ACC and ASME Dynamic Systems and Control Conference Best Student Paper Finalist (as student and advisor), the UC Presidential Postdoctoral Fellowship, the NSF Graduate Research Fellowship, the University of Michigan Distinguished ProQuest Dissertation Honorable Mention, the University of Michigan Rackham Merit Fellowship, and the College of Engineering Distinguished Leadership Award.